RNG2 tethers the conoid to the apical polar ring in *Toxoplasma gondii*: a key mechanism in parasite motility and invasion

Romuald Haase[1]#, Bingjian Ren[1]#, Nicolas Dos Santos Pacheco[1,2], Rémy Visentin[1], Bohumil Maco[1], Ricardo Mondragon Flores[3], Oscar Vadas[1]*, Dominique Soldati-Favre[1]*

# These authors contributed equally

Affiliation:

[1]Department of Microbiology and Molecular Medicine, Faculty of Medicine, University of Geneva

[2] Present address: Department of Biochemistry, University of Cambridge, Cambridge, United Kingdom.

[3]Department of Biochemistry, Center for Research and Advanced Studies of the National Polytechnic Institute, Mexico City

Corresponding authors: dominique.soldati-favre@unige.ch; oscar.vadas@unige.ch

Short title: **Apical anchoring of *Toxoplasma gondii* conoid**

Abbreviations: SPMTs, ICMTs, BFs, IMC, U-ExM, iU-ExM, IEM, SEC

Keywords

Apicomplexa, *Toxoplasma gondii*, apical polar ring, conoid, subpellicular microtubules, conoid extrusion, motility, invasion, egress, ultrastructure expansion microscopy

Abstract

In *Toxoplasma gondii*, the conoid is a dynamic organelle composed of spiraling tubulin fibers that extrudes during egress, gliding motility, and invasion. This organelle traverses the apical polar ring (APR) in response to calcium waves and plays a critical role in controlling parasite motility. While the actomyosin-dependent extrusion of the conoid is beginning to be understood, the mechanism by which it is anchored apically to the APR remains unclear. RNG2, a protein localized at both the conoid and the APR, has emerged as a key candidate for this function. By combining iterative ultrastructure expansion microscopy and immunoelectron microscopy we discovered that RNG2 forms 22 tethers between the APR and the conoid. The unique biochemical properties of RNG2, including several proteolytic processing events and its ability to form concatenations, enable it to function as a dynamic bridge between these structures. Conditional depletion of RNG2 resulted in the conoid organelle detaching from the APR without compromising the integrity of its structure, thereby confirming RNG2 essential tethering role. Although microneme secretion remains normal, parasites lacking RNG2 were unable to move and impaired in rhoptry discharge, highlighting the conoid's crucial role in parasite motility and invasion. RNG2 is a pivotal protein that ensures conoid functionality in *Coccidia*.

Introduction

The phylum Apicomplexa comprises single-cell eukaryotic parasites of high medical relevance, most notably *Plasmodium* spp., *Cryptosporidium* spp., and *Toxoplasma gondii* [1]. Members of this phylum share an elaborate apical complex composed of specialized secretory organelles called rhoptries and micronemes, as well as tubulin-based cytoskeletal elements [2, 3]. The apical complex critically coordinates organelle secretion and activation of the actomyosin system to drive gliding motility, invasion, and egress from infected cells [4, 5].

The shape of *T. gondii* is determined by scaffolding components, including the inner membrane complex (IMC), the alveolin network and the subpellicular microtubules (SPMTs), which collectively provide rigidity to the parasite [6, 7] (Fig. 1). The 22 SPMTs extend approximately two-thirds of the parasite length and emerge from a protein-based structure called the apical polar ring (APR) [8, 9] (Fig. 1). The conoid consists of a cone of spiraling tubulin fibers [10], surmounted by two preconoidal rings (PCRs) serving as hubs for the assembly of the gliding machinery [11]. The inside of the conoid hosts two short intraconoidal microtubules (ICMTs) [10] with aligned microtubule-associated vesicles predicted to participate in rhoptry discharge [12-14] (Fig. 1). The conoid is a dynamic organelle that extrudes and retracts through the APR in response to changes in intracellular calcium levels [15, 16]. Conoid extrusion relies on F-actin produced by formin 1 (FRM1) positioned at the PCRs, and is powered by myosin H (MyoH), anchored to the cone [11]. The dynamics of the conoid serve as a gatekeeper for the entry of F-actin in the pellicular space, between the IMC and plasma membrane, to reach other glideosome components, such as myosin A (MyoA), and sustain parasite forward motion [11, 17]

The APR is assumed to act as an atypical microtubule organizing center (MTOC) for the SPMTs [8, 9]. Several mutants that lead to the loss of APR result in disorganization of the SPMTs and disappearance of the conoid [7, 18-21]. Only a few APR proteins have been identified to date in *T. gondii*. KinesinA (KinA) is an early marker of APR, whereas APR1 and RNG1 appear later during daughter cell formation [18, 22]. Individual protein downregulation has a minimal effect on parasite replication; however, simultaneous depletion of KinA and APR1 resulted in the loss of the APR, disorganized SPMTs and drastic defects in gliding motility and invasion [18]. Similarly, depletion of RNG2 was previously reported to alter microneme secretion, leading to motility and invasion defects [23]. Interestingly, RNG2 exhibits an atypical dual localization, with the carboxy-terminus positioned to the APR and the amino-terminus localized to the conoid [23].

92 The use of recombinantly produced RNG2 shows that the protein is self-processed and prone
93 to oligomerization, supporting a model of APR-conoid tethering that is compatible with rapid
94 extension and shrinking distances. Iterative U-ExM applied to RNG2 and immunoelectron
95 microscopy (IEM) using polyclonal anti-RNG2 antibodies confirmed that this protein spans
96 the gap between the conoid and the APR. Of relevance, 22 binding fibers (BFs) were previously
97 visualized by electron microscopy and postulated to assist conoid extrusion [24]. Conditional
98 depletion of RNG2 results in the dramatic conoid detachment from the apical pole, further
99 supporting its role in tethering the conoid to the APR which is critical retraction to keep the
100 organelle in place
101

102 ## Results

103 **RNG2 is self-processed and oligomerizes in vitro**

104 *RNG2* codes for a 290 kDa protein that encompasses a tropomyosin domain (Tropo) within a
105 long coil-coiled region flanked by disordered N- and C-terminal ends (Fig 2A). To decipher
106 the biochemical properties of RNG2, we expressed recombinant full length and truncated
107 RNG2 variants with an N-terminal His-Tag and a C-terminal TwinStrep-Tag in Sf9 insect cells
108 (Fig 2A). All RNG2 constructs showed robust expression; however, only the ΔN+CTer variant
109 exhibited good solubility (Fig 2B). Full-length RNG2 was completely insoluble, whereas the
110 ΔNTer, ΔTropo, and ΔCTer variants showed partial solubility (Fig 2B-C). Western blot
111 analysis with anti-His and anti-Strep antibodies further highlighted the presence of both N- and
112 C-terminally truncated fragments for almost all the variants (Fig 2C). Only the ΔNTer variant
113 did not display any processing, with a single band detected with anti-His and anti-Strep
114 antibodies corresponding to the predicted size of the protein (Fig 2C).
115 Purification via the N-terminal His-Tag was not achievable for any of the constructs. In contrast,
116 purification by pulling on the C-terminal Strep-Tag proved successful for RNG2 constructs
117 where the C-terminal 300 residues were truncated (ΔCTer and ΔN+CTer RNG2), moreover
118 requiring salt concentrations largely exceeding physiological conditions (800 mM NaCl).
119 Affinity-purified proteins were subjected to size exclusion chromatography (SEC), and the
120 fractions were analyzed by SDS–PAGE, mass spectrometry, and western blotting. For both C-
121 terminally truncated constructs, purification led to the isolation of the same three main products
122 with sizes corresponding to 155 kDa, 90 kDa, and 60 kDa (Fig 2D, S1A-B Fig). All the
123 fragments coeluted in the void volume of the SEC, corresponding to molecule sizes greater
124 than 600 kDa, indicating that the fragments formed large oligomers (Fig 2D, S1A-B Fig).

125 Western blot analysis confirmed that all the purified products had lost the N-terminal His-Tag
126 (S1B Fig). This provides an explanation for the failure to isolate RNG2 fragments by using the
127 N-terminal His tag and strongly suggests that these fragments are self-processed. Mass
128 spectrometry (MS) analysis confirmed that the purified material corresponded to RNG2
129 fragments and allowed mapping of the fragment boundaries (Fig 2D, S1C Fig).
130 To isolate homogeneous RNG2 truncated proteins, each of the 155, 90 and 60 kDa fragments
131 was individually expressed and purified via the same workflow as described earlier. Like the
132 larger constructs, each fragment eluted in the void volume by SEC, indicating oligomerization
133 (S1D Fig). To test whether fragments of different sizes could form hetero-oligomers, pull-down
134 experiments were performed. Different pairs of purified fragments were mixed and pulled
135 down by affinity purification using a tag present only on one of the fragments (Fig 2E). None
136 of the fragments coeluted with a partner, indicating that preformed homo-oligomers cannot
137 assemble into hetero-oligomers (Fig 2E).
138 Collectively, heterologous expression of RNG2 provided evidence that the protein is highly
139 self-processed. Only a mixture of truncated RNG2 constructs could be purified, which were
140 associated with large homo-oligomers containing fragments of 155, 90 and 60 kDa.
141
142 **RNG2 forms 22 tethers between the conoid and the APR**
143 Double epitope tagging at both extremities of RNG2 previously revealed that the N-terminal
144 tag stains the conoid, whereas the C-terminal tag labels the APR [23]. To resolve this
145 conundrum and scrutinize the biochemical properties of RNG2 in *T. gondii*, we introduced
146 epitope tags at the N-terminus (Myc), center (Ty), and C-terminus (HA) along with a C-
147 terminal mAID cassette (Fig. 3A). The endogenous triple epitope-tagged RNG2 clonal line was
148 confirmed by genomic PCR (S2A Fig) and western blot analysis (Fig. 3B). Several RNG2
149 truncated products of high molecular weight were detected with anti-HA and anti-Ty
150 antibodies. The specificity of those bands was confirmed by their disappearance in parasites
151 treated with auxin (IAA). However, the anti-Myc antibody detected only the full-length version
152 of RNG2, which is consistent with N-terminal processing events (Fig 3B).
153 Indirect immunofluorescence assay (IFA) using the three antibodies (Myc, Ty, HA) confirmed
154 the apical localization of the RNG2 as well as tight regulation under auxin treatment (S2B Fig).
155 To refine the dynamic behavior of RNG2, the position of the different tags was assessed via
156 U-ExM on extracellular tachyzoites on extruded or retracted conoids (Fig. 3C). The N-terminus
157 of RNG2 (Myc) was found at the base of the conoid both in extruded and retracted states,
158 whereas the C-terminus (HA) was always localized on top of the SPMTs at the APR level,

159 confirming previous observations [23]. The central Ty tag localized between the conoid base
160 and SPMTs, which was further confirmed through dual localization with the N- and C-terminal
161 tags (Fig. 3D). Interestingly, the Ty-Tag colocalized with the N-terminal Myc-Tag only when
162 the conoid was retracted, suggesting a shortening of the protein length in the retracted state
163 (S2C Fig). Taken together, these data confirm the dual localization of RNG2 [23] and suggest
164 that the protein spans the gap between APR and conoid.
165 To achieve higher resolution, we employed iterative expansion microscopy (iU-ExM), which
166 allows for a 16-fold expansion ratio compared with the 4-fold expansion ratio of U-ExM [25].
167 With increased resolution, we observed that the RNG2 C-terminus forms 22 puncta that align
168 with the tips of SPMTs, as well as 22 puncta on the conoid looking at the RNG2 N-terminus
169 (Fig. 3E). In parallel, we raised anti-RNG2 polyclonal antibodies in rabbit by injecting the
170 purified RNG2- ΔCTer fragments described earlier (Fig 2D). The anti-RNG2 antibodies
171 showed very high specificity for RNG2 according to both U-ExM and by western blot analysis
172 (S3A-B Fig). In line with our previous observations, the antibodies covering the central region
173 of the protein decorated the space between the conoid and SPMTs (S3A Fig) and between the
174 signals of Myc and HA-Tags (S3C Fig).
175 Recently, electron microscopy (EM) ultrastructural analysis revealed the existence of binding
176 fibers (BFs) organized in a cartwheel-like conformation and linking the conoid to the SPMTs
177 [24]. To test whether RNG2 could be a component of BFs, we performed immunoelectron
178 microscopy (IEM) with rabbit anti-RNG2 antibodies (Fig. 3F). Although BFs were detected in
179 the cytoskeleton only as an ultrastructure control (Fig. 3F), in the cytoskeletons processed for
180 IEM, many of the fibers disappeared likely because of the numerous washes and incubations
181 with the antibodies. However, a large accumulation of gold labels was found in the space
182 between the conoid and APR and in some BFs still visible in the preparations (Fig. 3F). Taken
183 together, the iU-ExM- and IEM-based evidence for the spread of RNG2 between the APR
184 support the role of RNG2 as a component of the 22 BFs.
185
186 **RNG2 critically maintains the conoid attached to the APR during retraction**
187 Considering the biochemical and imaging observations supporting the role of RNG2 in conoid
188 attachment to the APR, we revisited its function, taking advantage of the fast depletion of the
189 protein with the auxin degron system. RNG2 depletion by IAA, as well as full deletion of the
190 gene (RNG2-KO), were confirmed to be fitness conferring by plaque assays (S4A Fig). Conoid
191 extrusion can be triggered by artificial elevation of cGMP levels with BIPPO, a
192 phosphodiesterase (PDE) inhibitor [26] and unambiguously observed by U-ExM and EM [11,

193 26, 27]. Strikingly in BIPPO-stimulated extracellular RNG2-depleted parasites, the conoid
194 detached from the apex of the cell and was found floating in the parasite cytosol both by U-
195 ExM and EM (Fig. 4A-B). Importantly, conoid detachment was prominently observed in more
196 than 80% of BIPPO-stimulated extracellular parasites. To determine whether actomyosin-
197 driven conoid extrusion triggers conoid detachment, we performed a conoid extrusion assay
198 using parasites pretreated with an inhibitor of actin polymerization, cytochalasin D (CD) [11].
199 Under normal conditions, BIPPO stimulation resulted in more than 84% of parasites exhibiting
200 conoid extrusion, whereas treatment with CD almost completely inhibited extrusion, with 95%
201 of parasites showing a retracted conoid (Fig. 4C). However, in RNG2-depleted parasites, only
202 9% of stimulated parasites displayed an extruded conoid, while 77% exhibited conoid
203 detachment. In contrast, when treated with CD, most RNG2-depleted parasites maintained a
204 retracted conoid, like the parental strain (Fig. 4C). These findings suggest that conoid extrusion
205 must be stimulated to observe the detachment caused by RNG2 depletion. Imaging of the
206 detached conoid via EM revealed that the organelle remained intact with PCRs and ICMTs still
207 associated with the tubulin cone (Fig. 4B). Additionally, the electron-dense structure capping
208 the 22 SPMTs like a rubber-band, was unaffected (Fig. 4A). The consistent localization and
209 expression levels of conoid and APR markers, conoid protein hub 1 (CPH1) and APR1 [18,
210 28] , respectively further validated these structural observations (Fig. 4AD). Taken together,
211 these findings demonstrate that RNG2 plays a critical role in retaining the conoid at the apical
212 pole following its extrusion.
213
214 **Detachment of the conoid in absence of RNG2 impairs motility and positioning of the**
215 **rhoptries**
216 *T. gondii* tachyzoites possess eight to twelve rhoptries, with two of them having their necks
217 docked inside the conoid and primed for exocytosis (Mageswaran et al., 2021). Micronemes
218 similarly accumulate at the apical pole of the parasite (Dubois and Soldati-Favre, 2019). Since
219 the conoid is assumed to serve as funnel for the secretion of microneme and rhoptry contents,
220 we assessed the impact of conoid detachment on these processes. Induced microneme secretion
221 showed no significant defect following conditional depletion of RNG2 (Fig. 4E). Consistent
222 with this observation, RNG2-depleted parasites were able to successfully egress, lysing both
223 the parasitophorous vacuole membrane (PVM) and the plasma membrane of the infected host
224 cell upon BIPPO stimulation (Fig. 4F). However, RNG2-depleted parasites remained clustered
225 at the site of host cell lysis, indicating an impairment in motility and dissemination. This was
226 confirmed by a severe defect in the gliding trail assay (S4B Fig). Interestingly, U-ExM revealed

227 that some micronemes were still associated to the detached conoid, pointing to the existence of
228 physical interactions between the conoid and these organelles (Fig. 4G). More strikingly the
229 rhoptries were considerably disorganized in RNG2-depleted parasites (Fig. 4G). Given that
230 proper rhoptry positioning is crucial for their exocytosis, we assessed the ability of the parasites
231 to discharge their rhoptry contents into the host cell in the absence of RNG2. Rhoptry secretion
232 was measured by monitoring the phosphorylation of host cell nuclear STAT-6, a marker for
233 rhoptry discharge [29]. In ASP3-knockdown parasites, used as a negative control, rhoptry
234 secretion was shown to be entirely blocked. In contrast, RNG2-knockdown parasites exhibited
235 a 50% reduction in rhoptry discharge, which was comparable to that observed in Δrng2 mutant
236 (Fig. 4H) [30]. Consequently, depletion of RNG2 resulted in a reduction of invasion efficiency
237 to less than half of that seen in the parental strain (S4C Fig).
238 To conclude, the disconnection of the conoid from the APR led to improper localization of the
239 rhoptries, which adversely affected the parasite's invasion capacity. Although microneme
240 secretion and PVM rupture were not impacted in RNG2-depleted parasites, the detachment of
241 the conoid and its PCRs deprived the parasite of apical F-actin polymerization resulting in a
242 profound motility defect.
243
244 **The central region of RNG2 is critical for conoid tethering at the apical pole**
245 The coiled-coil region in the central part of RNG2 expands more than two-thirds of the protein
246 length and contains a putative tropomyosin motif insert (Fig 5A). The N-terminal 500 residues
247 and C-terminal 300 residues of RNG2 have no identifiable structure or motifs. To investigate
248 whether RNG2 subdomains are involved in conoid tethering, the *Δrng2* cell line was
249 complemented with truncated versions of the protein expressed under the control of the tubulin
250 promoter. Western blot analysis confirmed the expression of each variant at the expected size,
251 as well as the presence of processed forms like those observed for the endogenous protein (Fig.
252 5B). IFA and U-ExM of all the truncated proteins confirmed APR localization, with an
253 additional signal in the cytoplasm likely due to overexpression (Fig. 5C, S5A Fig). Plaque
254 assays were performed to assess the fitness of the complemented lines. The overexpression of
255 the full length, ΔNTer, and ΔTropo variants fully rescued the fitness of parasites following the
256 depletion of endogenous RNG2 (Fig. 5D, S5A Fig). However, the ΔCTer and ΔN+CTer
257 variants only partially restored parasite fitness, indicating that the C-terminal region of RNG2
258 plays a critical role in its physiological function, whereas the N-terminal region and the central
259 tropomyosin domain are dispensable (Fig. 5D, S5A Fig). Consistent with the plaque assay
260 findings, the ΔCTer- and ΔN+CTer-complemented strains exhibited mild invasion defects,

261 whereas the WT and ΔTropo strains fully complemented the initial invasion defect (Fig. 5E).
262 Notably, the ΔNTer variant showed a slight but significant reduction in invasion (10%
263 reduction).
264 Examination of conoid detachment in the various RNG2 variants revealed that in the Δrng2
265 strain, over 90% of the conoids were detached from the APR, while in the TIR1 parental strain,
266 fewer than 3% of conoids were detached, possibly due to artifacts from U-ExM (Fig. 5F). The
267 wild-type and ΔTropo variants successfully complemented the depletion of endogenous RNG2,
268 resulting in very few detached conoids. In contrast, 50% of conoids in the ΔCTer and ΔN+CTer
269 variant-complemented strains were detached from the APR (Fig. 5F). Although the ΔNTer
270 strain did not show a significant fitness defect, 20% of its conoids were detached, which
271 corresponds with the slightly impaired invasion phenotype observed (Fig. 5F). Following
272 conoid extrusion, the protein variants either remained tethered to the APR (as seen with ΔNTer)
273 or were associated with the floating conoids (as observed with the ΔCTer variant or in strains
274 with both N- and C-terminal truncations). This suggests that the N-terminal region of RNG2 is
275 associated with the detached conoid, while the C-terminal region interacts with the APR (Fig.
276 5G).
277 Having established that the N- and C-terminal extremities of RNG2 are required to bind with
278 the conoid and APR, respectively, we explored the internal sequence that might mediate
279 oligomerization. To this end, two additional RNG2 variants were engineered: one featuring an
280 extended central region with six tropomyosin domain repeats (RNG2-6Tropo) and another
281 shorter variant where most of the internal sequence was removed (RNG2-ΔCenter) (Fig. 5H).
282 Both variants were dually tagged with Myc-tags and Ty-Tags at their N- and C-terminal ends,
283 respectively. Western blot analysis confirmed that both variants were expressed correctly and
284 exhibited several processed forms, particularly in the extended RNG2 protein (Fig. 5I).
285 Comparison of the blots indicated the presence of several fragments of identical size between
286 the two variants, suggesting that a major N-terminal fragment of approximately 110 kDa and
287 two key C-terminal fragments of 60 and 40 kDa were produced (Fig. 5I). These fragments
288 likely correspond to the minimal regions essential for binding to the conoid and APR,
289 respectively. Both variants accumulated at the apical pole, as shown by IFA (S5C Fig). While
290 the 6Tropo variant fully complemented the *Δrng2* strain, the ΔCenter strain failed to
291 complement it leading to conoid detachment (Fig. 5J-K-L, S5B Fig). The 6Tropo variant dually
292 localized to the conoid and APR, likel RNG2 (Fig. 5M). In contrast, RNG2-ΔCenter localized
293 at both the conoid and APR when detected with antibodies recognizing either the N- or C-
294 terminal extremities, suggesting that the mutant protein is too short to span the gap between

295 the two structures (Fig. 5M). These observations establish that i) RNG2-ΔCenter is not
296 processed, leading to colocalization of the N- and C-termini; ii) The extremities of RNG2 are
297 sufficient for binding the conoid and APR but not for conoid tethering; and iii) The processing
298 and oligomerization of the central region of RNG2 are critical for tethering the conoid at the
299 apical pole.
300

301 **Discussion**

302 The conoid serves as a critical hub for assembling all the molecular machinery necessary for
303 parasite invasion. This dynamic cytoskeletal element orchestrates the discharge of secretory
304 organelles and the assembly of the actomyosin-based glideosome, which powers parasite
305 motility. Originally believed to be exclusive to cyst-forming parasites, the conoid has recently
306 been found in a broader range of Apicomplexans, including *Plasmodium* and *Cryptosporidium*
307 species [31-34].
308 In *T. gondii*, the conoid undergoes calcium-dependent extrusion and retraction through the
309 APR, a process crucial for controlling parasite motility by directing actin filaments into the
310 pellicular space, leading to myosin A-driven forward motion [11]. Despite this understanding,
311 the factors responsible for maintaining the conoid at the apical pole and facilitating its
312 movement through the APR remained unclear until recently. The identification of BFs acting
313 as flexible tethers between the APR and conoid provided the first physical link between these
314 structures [24].
315 RNG2 emerged as a strong candidate for APR attachment due to its dual localization between
316 the APR and conoid [23]. *In vitro* studies revealed that RNG2 is prone to self-processing and
317 oligomerization, with fragments localizing between the conoid and APR. The purified proteins
318 used to generate the RNG2 rabbit polyclonal antibody, which specifically recognizes the
319 processed products, were instrumental in leading us to conclude that RNG2 undergoes
320 processing within the parasites. This processing results in certain RNG2 fragments localizing
321 between the conoid and the APR. High-resolution imaging based on iU-ExM detected RNG2
322 as 22 puncta at the APR and conoid levels supporting its role as part of the BFs. Of relevance,
323 RNG2 depletion caused conoid detachment upon BIPPO stimulation, emphasizing its role in
324 anchoring the conoid. Notably, this detachment occurs after extrusion, as CD prevents
325 detachment, indicating that RNG2 is crucial for maintaining conoid positioning during and
326 after extrusion.

327 Microneme secretion remained unaffected in RNG2-depleted parasites, consistent with
328 previous observations that conoid extrusion is not required for secretion [11]. However, some
329 micronemes remained linked to the detached conoid, suggesting intrinsic microneme-binding
330 properties within the conoid. Three major regulators of microneme apical positioning and
331 exocytosis namely, HOOK, FTS and HIP, were previously shown to accumulate at the apical
332 pole [35]. While their precise localization within the apical pole remains elusive, investigations
333 of RNG2-depleted parasites could shed light on their ability to reach the conoid and possibly
334 explain how micronemes remains associated with the detached conoid.
335 The proper positioning of rhoptries, essential for their discharge, was disrupted by RNG2
336 depletion, explaining the significant reduction in rhoptry discharge observed in these parasites.
337 Recent studies have demonstrated that during rhoptry discharge, two rhoptries dock at the
338 apical vesicle (AV) located at the parasite membrane [36]. Given the proximity of the AV to
339 the PCRs that detach from the conoid, investigating the positioning of the AV upon conoid
340 detachment would be worthwhile.
341 Interestingly, RNG2 depletion did not abrogate the parasite's fitness entirely, with only a 50%
342 reduction in invasion observed. Despite normal microneme secretion and conoid extrusion,
343 RNG2-depleted parasites exhibited motility defects due to conoid detachment, preventing F-
344 actin translocation necessary for motility.
345 The critical role of the central region of RNG2 in tethering the conoid at the apical pole was
346 highlighted by the similarity in phenotypes between RNG2-ΔCenter constructs and RNG2-KO
347 parasites. The colocalization of RNG2-ΔCenter at both the conoid and APR, when antibodies
348 targeted either the N- or C-terminal regions, indicated that RNG2's self-processing is necessary
349 for proper tethering. However, the mechanism by which the N- and C-terminal regions of
350 RNG2 anchor themselves to the APR and conoid remains unclear. It is possible that RNG2
351 interacts directly with tubulin proteins, or alternatively, it may require interactions with specific
352 surface proteins on both the conoid and APR to facilitate this connection.
353 Based on localization and phenotypic data, a model is proposed where RNG2 maintains the
354 conoid at the apical pole through strong interactions between its N- and C-terminal binding to
355 conoid and APR, respectively (Fig. 6A-B). RNG2 self-processing generates small fragments
356 of its central region that form filaments to span flexibly the distance between the conoid and
357 APR. Notably, the depletion of APR1, which also leads to conoid detachment, suggests a
358 possible interaction between RNG2 and APR1, warranting further investigation (Leung et al.
359 2017).

360 Through a combination of biochemical assays, genetic manipulations, and cell imaging, the
361 pivotal role of RNG2 in connecting the conoid to the APR, while enabling dynamic transitions
362 between extrusion and retraction has begun to be resolved.
363

364 ## Materials and methods

365 **Parasite maintenance**

366 *T. gondii* tachyzoites were amplified from HFFs (ATCC) in Dulbecco's modified Eagle's
367 medium (DMEM, Gibco) supplemented with 5% fetal calf serum (FCS, Gibco), 2 mM
368 glutamine and 25 µg/ml gentamicin (Gibco). Parasites and HFFs were maintained at 37°C with
369 5% CO_2.

370 **Generation of transgenic cell lines**

371 a – Generation of RNG2-mAID (triple epitope-tagged strain)

372 The gene map of RNG2 was retrieved from the ToxoDB website [37] (www.toxodb.org) via
373 the accession number TGGT1_244470. A specific gRNA (guideRNA) was designed to target
374 the 3'UTR of the endogenous locus via the EuPaGDT tool (www.grna.ctegd.uga.edu) [38].
375 The sequence of the gRNA (AAGAGAAATTGCCTTCATGT) was inserted into pU6-
376 Universal (pU6-Universal was a gift from Sebastian Lourido, Addgene plasmid #52694) [39].
377 A repair fragment containing the mAID-HA cassette, and flanking regions was amplified via
378 PCR via KOD polymerase (Novagen, Merck) via the oligos and template listed in Table S1.
379 Freshly egressed RHΔKu80ΔTir1 (called Tir1) tachyzoites were transfected via
380 electroporation [40] with 40 µg pU6-Universal bearing the gRNA alongside 100 µL (2 PCRs
381 of 50 µL) of repair fragment containing the mAID-HA cassette and homology regions for the
382 gene. For enrichment of the transfected population, parasites carrying an HXGPRT cassette
383 were selected with 25 mg/ml mycophenolic acid (MPA) and 50 mg/ml xanthine. The parasites
384 were then cloned and inserted into p96w, and the clonality of the population was assessed via
385 integration PCR, as shown in S2A Fig.

386 To insert a 3Myc tag on the N-terminal side of the RNG2 gene, two gRNAs were designed to
387 target the 5'UTR of the gene (CAACCGTTCCATGTAAGGCC) and a few base pairs after the
388 START codon (TTCGGGAGACGTTTCTCCTA). The two gRNAs were inserted into the
389 NdeI linearized plasmid listed **in Table S1** via Gibson assembly. A repair fragment of
390 approximately 500 bases containing the 3-Myc-Tag inserted just after the start codon and
391 containing homology regions on each side was synthesized (g-block IDT DNA company). This

392 repair fragment was inserted into the pCR-Blunt-II-Topo vector (Thermo Fisher, K270020)
393 and then amplified via PCR via KOD polymerase in the same way as described previously.
394 Freshly egressed clonal parasites bearing the mAID-HA cassette were transfected via
395 electroporation as described previously and sorted via flow cytometry (Cas9-GFP). The
396 selected parasites were then cloned and inserted into p96w, and the clonality of the population
397 was assessed via PCR, as shown in S2A Fig.
398 To insert a 3Ty-Tag in the internal sequence of the RNG2 gene, a gRNA was designed to target
399 this specific region (GAAGGGCAGAAGAACTT) and was inserted into the pU6-universal
400 vector as described above. A repair fragment of approximately 500 bases containing the 3-Ty-
401 Tag inserted just after the in frame of the sequence and containing homology regions on each
402 side was synthesized (g-block IDT DNA company). This repair fragment was inserted into the
403 pCR-Blunt-II-Topo vector (Thermo Fisher, K270020) and then amplified via PCR via KOD
404 polymerase in the same way as described previously. Freshly egressed clonal parasites bearing
405 the N-Ter Myc-tag and mAID-HA cassette were transfected via electroporation as described
406 previously and sorted via flow cytometry (Cas9-GFP). The selected parasites were then cloned
407 and inserted into p96w, and the clonality of the population was assessed via PCR, as shown in
408 For all the assays involving AID-based conditional knockdown systems, protein depletion was
409 achieved by adding 500 µM auxin (IAA) [41].
410
411 **b– Generation of the RNG2-KO strain**
412 To generate the RNG2 knockout line, two gRNAs were designed to target the 5'UTR of the
413 gene (CAACCGTTCCATGTAAGGCC) and the 3'UTR of the gene
414 (TGTGTGTTCATACTCCCGTG). The two gRNAs were inserted into the NdeI linearized
415 plasmid listed in **supplementary table 1** via Gibson assembly. A repair fragment containing
416 the DHFR cassette as well as flanking regions on each side was amplified via PCR via KOD
417 polymerase. Freshly egressed RHΔKu80ΔTir1 (called Tir1) parasites were transfected via
418 electroporation as described previously. For enrichment of the transfected population, parasites
419 carrying the DHFR cassette were selected with 1 µg/ml pyrimethamine.
420 The selected parasites were then cloned and inserted into p96w, and the clonality of the
421 population was assessed via PCR, as shown in S2A Fig.
422
423 **c– RNG2 variant expression at the UPRT locus**
424 The variant wild-type RNG2 gene was synthesized into the pFastBac vector between the
425 BamHI and HindIII cloning sites (Genscript Company). The RNG2 gene was then subcloned

426 and inserted into the pTub-UPRT-G13-Ty vector between the EcoRI and AvrII restriction sites
427 and under the control of the tubulin promoter to generate the vector pTub-UPRT-RNG2-WT-
428 Ty [42]. For each of the RNG2 variants, specific restriction sites were placed alongside the
429 RNG2 gene sequence, allowing the insertion/deletion of the desired sequences.
430 For RNG2-ΔNter, pTub-UPRT-RNG2-WT-Ty was digested by the restriction enzyme EcoRI
431 + SpeI and ligated with the primer pairs listed in Table S1 to generate pUPRT-RNG2-ΔNter-
432 Ty.
433 For RNG2-ΔCter, pFastBac-RNG2-WT was digested by the restriction enzyme NotI to
434 generate pFastBac-RNG2-ΔCter. pFastBac-RNG2-ΔCter was then digested with EcoRI + XbaI
435 and cloned and inserted into pTub-UPRT-G13-Ty, which was subsequently digested with
436 EcoRI+AvrII to generate pTub-UPRT-RNG2-ΔCter-Ty. For RNG2-ΔN+Cter, pTub-UPRT-
437 RNG2-ΔCter-Ty was digested by the restriction enzyme EcoRI + SpeI and ligated with primer
438 pairs 10629/10630 to generate pTub-UPRT-RNG2-ΔN+Cter-Ty. For RNG2-ΔTropo,
439 pFastBac- RNG2-WT was digested by the restriction enzymes SalI + XhoI followed by
440 religation. The sequences were then digested by EcoRI + XbaI to clone into the EcoRI + AvrII
441 digested vector pUPRT-UPRT-G13-Ty to generate pTub-UPRT-RNG2-ΔTropo-Ty.
442 For RNG2-ΔCenter, the RNG2-ΔCenter variant was synthesized and cloned and inserted into
443 the pTWIST vector. Cloning was performed via the digestion of pTWIST-RNG2-ΔCenter by
444 EcoRI + HindIII and cloning into the vector pTub-MyoL-3Ty, which was digested by EcoRI
445 + HindIII to generate pTub-UPRT-RNG2-ΔCenter.
446 For RNG2-6Tropo, 6xTropo fragments were synthesized and cloned and inserted into the
447 pTWIST-vector. The 6xTropo fragments were recycled by using the enzymes SalI + XhoI and
448 cloned and inserted into the vector pFastBac-RNG2-WT digested with SalI + XhoI to generate
449 pFastBac-RNG2-6Tropo. pFastBac-RNG2-6Tropo was then digested by EcoRI + XbaI and
450 cloned and inserted into pTub-UPRT-RNG2-ΔCenter digested by MfeI + NheI to generate
451 pTub-UPRT-RNG2-6Tropo
452 For transfection, *Δrng2* parasites were electroporated with 40 µg of linearized plasmid
453 encoding the selected RNG2 variant together with 20 µg of Cas9-encoding plasmid targeting
454 the UPRT locus [43]. For enrichment of the transfected population, parasites were selected
455 with 5 µM 5-fluorodeoxyuridine (FUDR). The clonality of the parasite lines was assessed via
456 immunofluorescence, and correct expression was assessed via western blotting.
457
458 **Expansion microcopy**

459 For this study, the expansion microscopy protocol applied to *Toxoplasma gondii* tachyzoites
460 was followed as previously described [44]. Briefly, parasites resuspended in warm PBS
461 containing 10 μM BIPPO were seeded on 12 mm coverslips precoated with poly-D-lysin
462 (Gibco) for 10 min. After excess PBS was removed, the coverslips were incubated in PBS
463 containing 0.7% formaldehyde and 1% acrylamide for 3 h at 37°C. Polymerization of the
464 expansion gel was performed on ice and contained a monomer mixture (19% sodium
465 acrylate/10% acrylamide/0.1% bis-acrylamide), 0.5% ammonium persulfate (APS) and 0.5%
466 tetramethylenediamine (TEMED). Fully polymerized gels were denatured at 95°C for 90 min
467 in denaturation buffer (200 mM SDS, 200 mM NaCl, 50 mM Tris, pH = 9) and expanded in
468 pure H_2O overnight.
469 The next day, the expansion ratio of the fully expanded gels was determined by measuring the
470 diameter of the gels. The well-expanded gels were shrunk in PBS and stained with primary and
471 secondary antibodies diluted in freshly prepared 2% PBS/BSA at 37°C for 2 h. Three washes
472 with PBS/0.1% Tween for 10 min were performed after primary and secondary antibody
473 staining. The stained gels were expanded again in pure H_2O overnight for further imaging. All
474 U-ExM images used in this study were acquired via Leica TCS SP8 microscope with the lens
475 HC PL Apo 100x/1.40 Oil CS2. Images were taken with Z-stacks and deconvolved with the
476 built-in setting of Leica LAS X. Final images were processed with ImageJ, and the maximum
477 projected images are presented in this study.
478
479 **Plaque assay**
480 HFF monolayers were infected with a serial dilution of *T. gondii* tachyzoites and grown for
481 seven days at 37 °C. The cells were fixed with paraformaldehyde-glutaraldehyde for 10 min,
482 followed by neutralization with 0.1 M PBS/glycine. The fixed monolayer was then stained with
483 crystal violet for 2 h and then washed three times with PBS.
484
485 **Conoid extrusion assay**
486 To induce conoid extrusion, freshly egressed tachyzoites were incubated with 10 μM BIPPO
487 for 10 min at room temperature. The parasites were then transferred to poly-D-lysine-coated
488 coverslips, followed by an expansion microscopy protocol as described previously. The conoid
489 status of a minimum of 100 parasites was determined for quantification. The data presented in
490 this study were acquired from three biological replicates.
491
492 **Invasion assay**

493 Coverslips covered with the HFF monolayer were infected with *T. gondii* tachyzoites,
494 centrifuged at 1200 × g for 1 min and incubated at 37 °C for 30 min. Infected HFFs were fixed
495 with paraformaldehyde-glutaraldehyde and neutralized with PBS/0.1 M glycine. The fixed
496 samples were blocked with 5% PBS-BSA for 20 min at room temperature, followed by 1 h of
497 staining with anti-SAG1 antibody and three washes in PBS. The stained samples were fixed
498 again with 1% formaldehyde for 7 min and permeabilized with PBS/0.2% Triton X-100 for 20
499 min. The samples were then stained with anti-GAP45 antibody and secondary antibodies. At
500 least 100 parasites per condition were counted to determine the invasion ratio. The data
501 presented in this study were from three biological replicates.
502
503 **Microneme secretion assay**
504 Freshly egressed parasites (syringed out in the case of parasites with severe egress defects)
505 were washed twice in warm DMEM, pelleted and resuspended in media containing 10 μM
506 BIPPO. The suspensions were incubated at 37°C for 15 min and centrifuged at 2000 × g to
507 allow separation of the pellet/supernatant (ESA) fraction. The isolated ESA fractions were
508 further centrifuged to remove any remaining cell debris. All the samples were subjected to
509 western blot analysis with anti-MIC2, anti-catalase and anti-GRA1 antibodies.
510
511 **Egress Assay**
512 Fresh tachyzoites were used to infect HFF on coverslips, which were subsequently cultured for
513 30 h at 37 °C. Infected cultures were incubated with DMEM containing BIPPO (10 μM) for
514 10 min at 37 °C, followed by PFA/Glu fixation and neutralization with 0.1 M PBS/glycine. The
515 coverslips were stained as described previously with the anti-GAP45 antibody and anti-GRA3.
516 At least 100 vacuoles per condition were counted. The data presented in this study were
517 acquired from three biological replicates.
518
519 **Gliding trail assay**
520 Freshly egressed tachyzoites were resuspended in warm DMEM containing 10 μM BIPPO,
521 seeded on 12 mm coverslips coated with poly-L-lysine, and centrifuged at 1200 × g for 2 min.
522 The plates with coverslips were incubated for 30 min at 37°C and fixed/stained as described.
523 The anti-SAG1 antibody was resuspended in 2% PBS/BSA, and the corresponding fluorescent
524 secondary antibody was used for visualization by imaging.
525
526 **STAT-6 rhoptry secretion assay**

527 A total of 5 × 10^6 freshly egressed parasites were harvested and resuspended in 250 µl of
528 DMEM for infection of one coverslip seeded with an HFF monolayer. After 30 seconds of
529 centrifugation at 1000 × g, the coverslips were incubated at 37°C for 20 min, followed by 8
530 min of fixation in ice-cold methanol (MeOH). After 30 min of blocking with 5% PBS/BSA,
531 the coverslips were incubated overnight at 4°C with a STAT6-P antibody. The next day, the
532 coverslips were visualized with a fluorescent secondary antibody and DAPI. The rhoptry
533 discharge efficiency was determined by the ratio of the number of STAT6-P-positive cell nuclei
534 to the total number of nuclei (visualized by DAPI). At least 200 cell nuclei were counted for
535 quantification. The data presented in this study were acquired from three biological replicates.
536

537 **Baculovirus-infected Insect cell expression and purification**

538 All recombinant RNG2 proteins were expressed in Sf9 insect cells and purified following a
539 similar protocol. All the plasmids encoding RNG2 possessed an N-terminal His10-tag followed
540 by a TEV recognition sequence and an HRV-3C recognition sequence followed by a
541 TwinSTREP tag. Baculoviruses were generated following standard procedures, and the cells
542 were infected for 48 h at 27°C in a shaking incubator. Purifications were performed via a
543 combination of STREP-tactin affinity purification and size-exclusion chromatography. Briefly,
544 a pellet from 600 ml of cells was resuspended in 120 ml of lysis buffer (PBS supplemented
545 with 800 mM NaCl, 1 mM EDTA, 0.1% Triton X-100 and 3 mM beta-mercaptoethanol) and
546 lysed by shear force using a LM-20 microfluidizer set at 20,000 psi. The lysate was centrifuged
547 at 35,000 × g for 35 min at 4°C, and the supernatant was applied to a 5 ml STREP-TACTIN
548 XT 4Flow column (IBA) at 0.5 ml/min. The column was washed with 50 ml of lysis buffer and
549 eluted with 15 ml of lysis buffer supplemented with 50 mM biotin. The eluted protein was
550 concentrated to 1 ml via a 30 MWCO Amicon concentrator and loaded on a Superdex 200
551 10/300 GL column at 22°C previously equilibrated in PBS supplemented with 3 mM DTT.
552 Fractions were analyzed via SDS–PAGE, pooled and flash frozen in liquid nitrogen before
553 being stored at -80°C.
554

555 **Western blot analysis for monitoring auxin-induced protein degradation**

556 HFF monolayers seeded in 6 cm petri dishes were infected with freshly egressed parasites and
557 grown for 48 h in the absence or presence of IAA (500 µM). The parasites were pelleted at
558 1200 rpm, resuspended in protein loading buffer containing 2% SDS and boiled for 15 min at
559 95°C. To monitor the depletion over various periods, the HFF monolayer was infected with
560 freshly egressed parasites for 1 h at 37 °C. The extracellular parasites were then washed with

561 DMEM supplemented with 500 μM IAA for 1, 2, 4, 8, or 12 h. After 12 h of depletion, all the
562 samples were pelleted and resuspended in SDS. Protein depletion was assessed by Western
563 blotting using an anti-HA antibody against the protein of interest and anti-MIC2 as a loading
564 control.
565
566 **Electron microscopy**
567 Extracellular tachyzoites were prepared in the same manner as previously described [19].
568 Briefly, the extracellular parasites were pelleted in PBS. Conoid extrusion was induced by
569 incubation with 40 μl of BIPPO in PBS for 5 min at 37 °C. A 4 μl sample was applied to a
570 glow-discharged 200-mesh Cu electron microscopy grid for 10 min. The excess sample was
571 removed by blotting with filter paper and immediately washed three times in double-distilled
572 water. Finally, the sample was negatively stained with a 0.5% aqueous solution of
573 phosphotungstic acid for 20 s and air-dried. Electron micrographs of parasite apical poles were
574 collected with a Tecnai 20 transmission electron microscope (FEI, Netherland) operated at an
575 acceleration voltage of 80 kV and equipped with a side-mounted CCD camera (MegaView III,
576 Olympus Imaging Systems) controlled by iTEM software (Olympus Imaging Systems).
577
578 **Immunoelectron microscopy**
579 The isolation of the cytoskeleton from tachyzoites of *T. gondii* was performed as previously
580 reported [24]. Briefly, a suspension of tachyzoites (1×10^6/ml) suspended in PHEM solution
581 (10 mM HEPES, 10 mM EGTA, 1 mM $MgCl_2$, 50 μg/ml N-Tosyl-L-phenylalanine
582 chloromethyl ketone, 50 μg/ml Nα-p-Tosyl-L-lysine chloromethyl ketone, and 17.4 μg/ml
583 phenylmethylsulfonyl fluoride, pH 6.9) was exposed to 0.1% Triton X-100 in PHEM for 1 min
584 at RT. The cytoskeleton fraction was centrifuged at 200,000 × *g* for 15 min at 4°C. Under such
585 conditions, most of the cytoskeletons were integrated into the typical crescent shape of
586 tachyzoites. To isolate the cytoskeletons in a cartwheel-like conformation, tachyzoites were
587 exposed to Triton X-100 solution for 3 minutes. For immune-electron microscopy (IEM),
588 cytoskeletons were deposited on Ni grids covered with a formvar film (Polysciences,
589 Warrington, PA, USA), fixed with 1% PAF in PHEM, blocked with 0.1% BSA, and then
590 incubated for 2 h with anti-RNG2 (1:100 dilution) diluted in PHEM inside a humid chamber
591 at RT. After washing, the samples were incubated for 2 h with IgG goat anti-rabbit IgG
592 antibodies (ZYMED Laboratories Inc., San Francisco, CA) coupled to 10 nm colloidal gold
593 particles diluted in PHEM, washed with PHEM, counterstained with uranyl acetate and

594 examined via TEM. As a negative control, the cytoskeleton was incubated with preimmune
595 serum and then with a secondary antibody coupled to gold particles.

596 Acknowledgments

597 We are grateful to Paul Guichard, Virgnie Hamel and Vincent Louvel for their teaching and
598 advice for iterative expansion microscopy. We thank Monica E Mondragon Castelán and
599 Sirenia González Pozos for their help in processing the IEM. Micrographs were obtained at the
600 Electron Microscopy Facility (LaNSE, CINVESTAV-IPN, Mexico). We thank the team at the
601 Bioimaging Core Facility, François Prodon, Olivier Brun and Nicolas Liaudet, for their
602 technical assistance and imaging analysis. The project is funded by the Swiss National Science
603 Foundation to DSF (310030_215445 and CRSII5_198545).
604

605 Author contributions

606 D.S.-F., R.H., and B.R. conceptualized the project. D.S.-F., R.H., B.R., and O.V.
607 conceptualized the methodology, and R.H., B.R., O.V., R.V., N.D.S.P., R.M.F. and B.M.
608 performed the investigations. R.H., B.R. and O.V. performed the formal analysis, and R.H.
609 wrote the original draft. D.S.-F., O.V., N.D.S.P., B.R. and R.M.F. reviewed and edited the
610 manuscript. D.S.-F. and R.M.F acquired funding and obtained resources. All the authors
611 contributed to this article and approved the submitted version.
612

613 Competing interests

614 The authors declare that they have no competing interests.
615

616 Figure legends

617 **Fig 1. *Toxoplasma gondii* tachyzoite cell organization**
618 **Left panel:** general cell organization of *Toxoplasma gondii* tachyzoites. **Right panel:** Zoomed
619 view of the detailed apical complex. ICMTs: Intraconoidal microtubules. PCRs: Preconoidal
620 rings. APR: Apical Polar Ring. IMC: Inner Membrane Complex. PM: Plasma membrane.
621 Scheme modified from [3]
622

623 **Fig 2. Biochemical investigation of wild-type and processed RNG2**
624 **(A)** Representation of the RNG2 constructs expressed in SF9 insect cells. **(B)** Insect cell protein
625 expression and solubility of the RNG2 truncation variants, as assessed by Coomassie blue

626 staining. **(C)** Protein expression and solubility of RNG2 truncation variants were assessed via
627 western blotting. **(D)** Size-exclusion chromatography (SEC) chromatogram of the affinity-
628 purified RNG2-ΔN+CTer variant obtained via Strep-tactin purification. A Coomassie-stained
629 gel of the protein-containing fractions of the SEC is shown on the right. **(E)** Pull-down assay
630 of RNG2 fragments assessed by Coomassie blue staining.
631
632 **Fig 3. RNG2 spans between the APR and the conoid, forming 22 tethers**
633 **(A)** Illustration of endogenous tagging of RNG2, including three epitope tags and a minimal
634 auxin inducible (mAID) motif. Estimation of the protein length corresponding to the distance
635 coverage of the central part of the protein in linear conformation. **(B)** Protein depletion after 48
636 h of auxin (IAA) treatment assessed by western blot. **(C)** U-ExM image of the 3 locations of
637 RNG2-mAID depending on the tag insertion. Images were taken with extruded and retracted
638 conoids. Scale bar = 3 µm. **(D)** Colocalization of the Ty internal tag with the N-terminal (Myc)
639 or C-terminal (HA) tags. Scale bar = 3 µm. Plot profile analysis of the signal. **(E)** Iterative
640 expansion microscopy (iU-ExM) of the N-terminal (Myc), middle (Ty) and C-terminal (HA)
641 tags of RNG2-mAID. Scale bar = 3 µm. **(F) Left panel:** Electron microscopy images of the *T.*
642 *gondii* apical complex as an ultrastructure control. **Right panel:** Immunoelectron microscopy
643 images obtained with the α-RNG2 antibody. Red arrows = gold particles. Scale bar = 100 nm.
644
645 **Fig 4. RNG2 depletion leads to conoid detachment and rhoptry mislocalization**
646 **(A)** U-ExM images showing extruded conoid and detached conoid RNG2-mAID-depleted
647 parasites and RNG2-KO parasites. Scale bar = 3 µm. **(B)** Electron microscopy images of
648 negatively stained tachyzoites with extruded conoids and detached conoids in RNG2-mAID-
649 depleted parasites and RNG2-KO parasites. Scale bar = 500 nm. **(C)** Quantification of the
650 conoid state in three categories: extruded, retracted and detached. Under all conditions,
651 extracellular tachyzoites were triggered for conoid extrusion via BIPPO in the absence of auxin
652 (IAA) and with or without cytochalasin D (CD). N = 100 parasites in 3 biological replicates.
653 **(D)** U-ExM images of CPH1 (conoid marker) and APR1 (APR marker) without or without the
654 conoid detached from the APR. Scale bar = 3 µm. **(E)** Western blot analysis of BIPPO-triggered
655 microneme secretion. ESA = Excreted secreted antigens. **(F) Left panel:** quantification of
656 lysed parasitophorous vacuoles upon egress triggered by BIPPO. **Right panel:** representative
657 images of the egress assay. Scale bar = 20 µm. **(G)** U-ExM of secretory organelles, with MIC2
658 used as a microneme marker and RON9 used as a rhoptry neck marker. Images taken with the
659 conoid attached or detached from the APR. Scale bar = 3 µm. **(H)** Quantification of rhoptry

660 secretion was performed to assess STAT-6 phosphorylation. At least 200 cell nuclei were
661 counted for data plotting, n = 3. ATc = anhydrotetracycline.
662
663 **Fig 5. Investigation of RNG2 subdomain functions**
664 **(A)** Representation of the RNG2 variants expressed in the RNG2-KO background. **(B)** Western
665 blot analysis of the expression of RNG2 variants expressed in the RNG2-KO background. **(C)**
666 U-ExM images of the localization of the RNG2 variants. Scale bar = 1 μm. **(D)** Quantification
667 of the plaque sizes created by the different RNG2 strains via a plaque assay. Ten plaques were
668 measured per biological replicate. Three biological replicates were evaluated. **(E)**
669 Quantification of the percentage of invasion by the different RNG2 strains in the invasion
670 assay. One hundred parasites were measured per biological replicate. Three biological
671 replicates were evaluated. **(F)** Quantification of the percentages of conoid retraction, extrusion,
672 and detachment by the different RNG2 strains in the conoid detachment assay. One hundred
673 parasites were measured per biological replicate. Three biological replicates were evaluated.
674 **(G)** U-ExM images of the localization of the RNG2 variants under conditions in which the
675 conoid detached from the apical pole. Scale bar = 1 μm. **(H)** Representation of the second round
676 of RNG2 variants expressed in the RNG2-KO background. **(I)** Western blot analysis of the
677 expression of the second round of RNG2 variants expressed in the RNG2-KO background. **(J)**
678 Quantification of the plaque sizes created by second-round RNG2 variants via a plaque assay.
679 Ten plaques were measured per biological replicate. Three biological replicates were evaluated.
680 **(K)** Quantification of the percentage of invading cells in response to the second round of RNG2
681 overexpression via an invasion assay. One hundred parasites were measured per biological
682 replicate. Three biological replicates were evaluated. **(F)** Quantification of the percentage of
683 conoid retraction/extruded/detaching by the second round of the RNG2 variant in the conoid
684 detachment assay. One hundred parasites were measured per biological replicate. Three
685 biological replicates were evaluated. **(M)** U-ExM images of the localization of the second
686 round of RNG2 variants under conditions in which the conoid detached from the apical pole.
687 Scale bar = 1 μm.
688
689 **Fig 6. Proposed model for the role of RNG2 and conoid apical anchorage**
690 (**A**) Illustration of the consequences of RNG2 depletion on the apical complex structure of *T.*
691 *gondii* tachyzoites. **(B)** Illustration of the RNG2 molecular tethering model.
692
693 **References**

1. Adl SM, Leander BS, Simpson AGB, Archibald JM, Anderson OR, Bass D, et al. Diversity, Nomenclature, and Taxonomy of Protists. Systematic Biology. 2007;56(4):684-9. doi: 10.1080/10635150701494127.
2. Hu K, Johnson J, Florens L, Fraunholz M, Suravajjala S, DiLullo C, et al. Cytoskeletal components of an invasion machine--the apical complex of Toxoplasma gondii. PLoS Pathog. 2006;2(2):e13. Epub 2006/03/07. doi: 10.1371/journal.ppat.0020013. PubMed PMID: 16518471; PubMed Central PMCID: PMCPMC1383488.
3. Dos Santos Pacheco N, Tosetti N, Koreny L, Waller RF, Soldati-Favre D. Evolution, Composition, Assembly, and Function of the Conoid in Apicomplexa. Trends Parasitol. 2020;36(8):688-704. Epub 2020/06/04. doi: 10.1016/j.pt.2020.05.001. PubMed PMID: 32487504.
4. Paredes-Santos TC, de Souza W, Attias M. Dynamics and 3D organization of secretory organelles of Toxoplasma gondii. J Struct Biol. 2012;177(2):420-30. Epub 2011/12/14. doi: 10.1016/j.jsb.2011.11.028. PubMed PMID: 22155668.
5. Frénal K, Dubremetz J-F, Lebrun M, Soldati-Favre D. Gliding motility powers invasion and egress in Apicomplexa. Nature Reviews Microbiology. 2017;15(11):645-60. doi: 10.1038/nrmicro.2017.86.
6. Harding CR, Frischknecht F. The Riveting Cellular Structures of Apicomplexan Parasites. Trends Parasitol. 2020;36(12):979-91. Epub 2020/10/05. doi: 10.1016/j.pt.2020.09.001. PubMed PMID: 33011071.
7. Tosetti N, Dos Santos Pacheco N, Bertiaux E, Maco B, Bournonville L, Hamel V, et al. Essential function of the alveolin network in the subpellicular microtubules and conoid assembly in Toxoplasma gondii. Elife. 2020;9. Epub 2020/05/08. doi: 10.7554/eLife.56635. PubMed PMID: 32379047; PubMed Central PMCID: PMCPMC7228768.
8. Nichols BA, Chiappino ML. Cytoskeleton of Toxoplasma gondii. J Protozool. 1987;34(2):217-26. doi: 10.1111/j.1550-7408.1987.tb03162.x. PubMed PMID: 3585817.
9. Morrissette NS, Sibley LD. Cytoskeleton of apicomplexan parasites. Microbiol Mol Biol Rev. 2002;66(1):21-38; table of contents. Epub 2002/03/05. doi: 10.1128/mmbr.66.1.21-38.2002. PubMed PMID: 11875126; PubMed Central PMCID: PMCPMC120781.
10. Hu K, Roos DS, Murray JM. A novel polymer of tubulin forms the conoid of Toxoplasma gondii. J Cell Biol. 2002;156(6):1039-50. Epub 2002/03/20. doi: 10.1083/jcb.200112086. PubMed PMID: 11901169; PubMed Central PMCID: PMCPMC2173456.
11. Dos Santos Pacheco N, Brusini L, Haase R, Tosetti N, Maco B, Brochet M, et al. Conoid extrusion regulates glideosome assembly to control motility and invasion in Apicomplexa. Nature Microbiology. 2022;7(11):1777-90. doi: 10.1038/s41564-022-01212-x.
12. Segev-Zarko LA, Dahlberg PD, Sun SY, Pelt DM, Kim CY, Egan ES, et al. Cryo-electron tomography with mixed-scale dense neural networks reveals key steps in deployment of Toxoplasma invasion machinery. PNAS Nexus. 2022;1(4):pgac183. Epub 20220904. doi: 10.1093/pnasnexus/pgac183. PubMed PMID: 36329726; PubMed Central PMCID: PMCPMC9615128.
13. Mageswaran SK, Guerin A, Theveny LM, Chen WD, Martinez M, Lebrun M, et al. In situ ultrastructures of two evolutionarily distant apicomplexan rhoptry secretion systems. Nat Commun. 2021;12(1):4983. Epub 20210817. doi: 10.1038/s41467-021-25309-9. PubMed PMID: 34404783; PubMed Central PMCID: PMCPMC8371170.
14. Dos Santos Pacheco N, Tell i Puig A, Guérin A, Martinez M, Maco B, Tosetti N, et al. Sustained rhoptry docking and discharge requires Toxoplasma gondii intraconoidal microtubule-associated proteins. Nature Communications. 2024;15(1):379. doi: 10.1038/s41467-023-44631-y.

15. Mondrago R, Frixione E. Ca2+-Dependence of Conoid Extrusion in Toxoplasma gondii Tachyzoites. Journal of Eukaryotic Microbiology. 1996;43(2):120-7. doi: https://doi.org/10.1111/j.1550-7408.1996.tb04491.x.
16. Del Carmen MG, Mondragon M, Gonzalez S, Mondragon R. Induction and regulation of conoid extrusion in Toxoplasma gondii. Cell Microbiol. 2009;11(6):967-82. Epub 2009/05/07. doi: 10.1111/j.1462-5822.2009.01304.x. PubMed PMID: 19416276.
17. Martinez M, Mageswaran SK, Guérin A, Chen WD, Thompson CP, Chavin S, et al. Origin and arrangement of actin filaments for gliding motility in apicomplexan parasites revealed by cryo-electron tomography. Nat Commun. 2023;14(1):4800. Epub 20230809. doi: 10.1038/s41467-023-40520-6. PubMed PMID: 37558667; PubMed Central PMCID: PMCPMC10412601.
18. Leung JM, He Y, Zhang F, Hwang YC, Nagayasu E, Liu J, et al. Stability and function of a putative microtubule-organizing center in the human parasite Toxoplasma gondii. Mol Biol Cell. 2017;28(10):1361-78. Epub 2017/03/24. doi: 10.1091/mbc.E17-01-0045. PubMed PMID: 28331073; PubMed Central PMCID: PMCPMC5426850.
19. Nicolas Dos Santos Pacheco NT, Aarti Krishnan, Romuald Haase, Bohumil Maco, Catherine Suarez, Bingjian Ren, and Dominique Soldati-Favre. Revisiting the Role of Toxoplasma gondii ERK7 in the Maintenance and Stability of the Apical Complex. Mbio. 2021. doi: 10.1128/mBio.02057-21
20. Back PS, O'Shaughnessy WJ, Moon AS, Dewangan PS, Hu X, Sha J, et al. Ancient MAPK ERK7 is regulated by an unusual inhibitory scaffold required for Toxoplasma apical complex biogenesis. Proc Natl Acad Sci U S A. 2020;117(22):12164-73. Epub 2020/05/16. doi: 10.1073/pnas.1921245117. PubMed PMID: 32409604; PubMed Central PMCID: PMCPMC7275706.
21. Dos Santos Pacheco N, Tosetti N, Krishnan A, Haase R, Maco B, Suarez C, et al. Revisiting the Role of Toxoplasma gondii ERK7 in the Maintenance and Stability of the Apical Complex. mBio. 2021;12(5):e02057-21. doi: 10.1128/mBio.02057-21.
22. Tran JQ, de Leon JC, Li C, Huynh MH, Beatty W, Morrissette NS. RNG1 is a late marker of the apical polar ring in Toxoplasma gondii. Cytoskeleton (Hoboken). 2010;67(9):586-98. Epub 2010/07/27. doi: 10.1002/cm.20469. PubMed PMID: 20658557; PubMed Central PMCID: PMCPMC2998517.
23. Katris NJ, van Dooren GG, McMillan PJ, Hanssen E, Tilley L, Waller RF. The apical complex provides a regulated gateway for secretion of invasion factors in Toxoplasma. PLoS Pathog. 2014;10(4):e1004074. Epub 2014/04/20. doi: 10.1371/journal.ppat.1004074. PubMed PMID: 24743791; PubMed Central PMCID: PMCPMC3990729.
24. Díaz-Martin RD, Sandoval Rodriguez FE, González Pozos S, Gómez de León CT, Mondragón Castelán M, Mondragón Flores R. A comprehensive ultrastructural analysis of the Toxoplasma gondii cytoskeleton. Parasitology Research. 2022;121(7):2065-78. doi: 10.1007/s00436-022-07534-3.
25. Louvel V, Haase R, Mercey O, Laporte MH, Eloy T, Baudrier É, et al. iU-ExM: nanoscopy of organelles and tissues with iterative ultrastructure expansion microscopy. Nature Communications. 2023;14(1):7893. doi: 10.1038/s41467-023-43582-8.
26. Howard BL, Harvey KL, Stewart RJ, Azevedo MF, Crabb BS, Jennings IG, et al. Identification of Potent Phosphodiesterase Inhibitors that Demonstrate Cyclic Nucleotide-Dependent Functions in Apicomplexan Parasites. ACS Chemical Biology. 2015;10(4):1145-54. doi: 10.1021/cb501004q.
27. Dos Santos Pacheco N, Tosetti N, Krishnan A, Haase R, Maco B, Suarez C, et al. Revisiting the Role of Toxoplasma gondii ERK7 in the Maintenance and Stability of the Apical Complex. mBio. 2021;12(5):10.1128/mbio.02057-21. doi: 10.1128/mbio.02057-21.

28. Long S, Anthony B, Drewry LL, Sibley LD. A conserved ankyrin repeat-containing protein regulates conoid stability, motility and cell invasion in Toxoplasma gondii. Nat Commun. 2017;8(1):2236. Epub 2017/12/23. doi: 10.1038/s41467-017-02341-2. PubMed PMID: 29269729; PubMed Central PMCID: PMCPMC5740107.
29. Ong Y-C, Reese ML, Boothroyd JC. Toxoplasma Rhoptry Protein 16 (ROP16) Subverts Host Function by Direct Tyrosine Phosphorylation of STAT6*. Journal of Biological Chemistry. 2010;285(37):28731-40. d
30. Dogga SK, Mukherjee B, Jacot D, Kockmann T, Molino L, Hammoudi P-M, et al. A druggable secretory protein maturase of Toxoplasma essential for invasion and egress. eLife. 2017;6:e27480. doi: 10.7554/eLife.27480.
31. Koreny L, Zeeshan M, Barylyuk K, Tromer EC, van Hooff JJE, Brady D, et al. Molecular characterization of the conoid complex in Toxoplasma reveals its conservation in all apicomplexans, including Plasmodium species. PLoS Biol. 2021;19(3):e3001081. Epub 2021/03/12. doi: 10.1371/journal.pbio.3001081. PubMed PMID: 33705380; PubMed Central PMCID: PMCPMC7951837.
32. Guizetti J, Frischknecht F. Apicomplexans: A conoid ring unites them all. PLOS Biology. 2021;19(3):e3001105. doi: 10.1371/journal.pbio.3001105.
33. Martinez M, Mageswaran SK, Guérin A, Chen WD, Thompson CP, Chavin S, et al. Origin and arrangement of actin filaments for gliding motility in apicomplexan parasites revealed by cryo-electron tomography. Nature Communications. 2023;14(1):4800. doi: 10.1038/s41467-023-40520-6.
34. Guérin A, Strelau KM, Barylyuk K, Wallbank BA, Berry L, Crook OM, et al. Cryptosporidium uses multiple distinct secretory organelles to interact with and modify its host cell. Cell Host & Microbe. 2023;31(4):650-64.e6.
35. Dubois DJ, Chehade S, Marq JB, Venugopal K, Maco B, Puig ATI, et al. Toxoplasma gondii HOOK-FTS-HIP Complex is Critical for Secretory Organelle Discharge during Motility, Invasion, and Egress. mBio. 2023;14(3):e0045823. Epub 20230424. doi: 10.1128/mbio.00458-23. PubMed PMID: 37093045; PubMed Central PMCID: PMCPMC10294612.
36. Martinez M, Chen WD, Cova MM, Molnár P, Mageswaran SK, Guérin A, et al. Rhoptry secretion system structure and priming in Plasmodium falciparum revealed using in situ cryo-electron tomography. Nature Microbiology. 2022;7(8):1230-8. doi: 10.1038/s41564-022-01171-3.
37. Harb OS, Roos DS. ToxoDB: Functional Genomics Resource for Toxoplasma and Related Organisms. In: Tonkin CJ, editor. Toxoplasma gondii: Methods and Protocols. New York, NY: Springer US; 2020. p. 27-47.
38. Peng D, Tarleton R. EuPaGDT: a web tool tailored to design CRISPR guide RNAs for eukaryotic pathogens. Microbial Genomics. 2015;1(4). doi: https://doi.org/10.1099/mgen.0.000033.
39. Sidik SM, Hackett CG, Tran F, Westwood NJ, Lourido S. Efficient Genome Engineering of Toxoplasma gondii Using CRISPR/Cas9. PLOS ONE. 2014;9(6):e100450. doi: 10.1371/journal.pone.0100450.
40. Soldati D, Boothroyd JC. Transient Transfection and Expression in the Obligate Intracellular Parasite Toxoplasma gondii. Science. 1993;260(5106):349-52. doi: doi:10.1126/science.8469986.
41. Brown KM, Long S, Sibley LD. Conditional Knockdown of Proteins Using Auxin-inducible Degron (AID) Fusions in Toxoplasma gondii. Bio Protoc. 2018;8(4). Epub 2018/04/13. doi: 10.21769/BioProtoc.2728. PubMed PMID: 29644255; PubMed Central PMCID: PMCPMC5890294.

841 42. Sheiner L, Demerly JL, Poulsen N, Beatty WL, Lucas O, Behnke MS, et al. A
842 Systematic Screen to Discover and Analyze Apicoplast Proteins Identifies a Conserved and
843 Essential Protein Import Factor. PLOS Pathogens. 2011;7(12):e1002392. doi:
844 10.1371/journal.ppat.1002392.
845 43. Donald RG, Roos DS. Insertional mutagenesis and marker rescue in a protozoan
846 parasite: cloning of the uracil phosphoribosyltransferase locus from Toxoplasma gondii. Proc
847 Natl Acad Sci U S A. 1995;92(12):5749-53. doi: 10.1073/pnas.92.12.5749. PubMed PMID:
848 7777580; PubMed Central PMCID: PMCPMC41774.
849 44. Dos Santos Pacheco N, Soldati-Favre D. Coupling Auxin-Inducible Degron System
850 with Ultrastructure Expansion Microscopy to Accelerate the Discovery of Gene Function in
851 Toxoplasma gondii. In: de Pablos LM, Sotillo J, editors. Parasite Genomics: Methods and
852 Protocols. New York, NY: Springer US; 2021. p. 121-37.
853

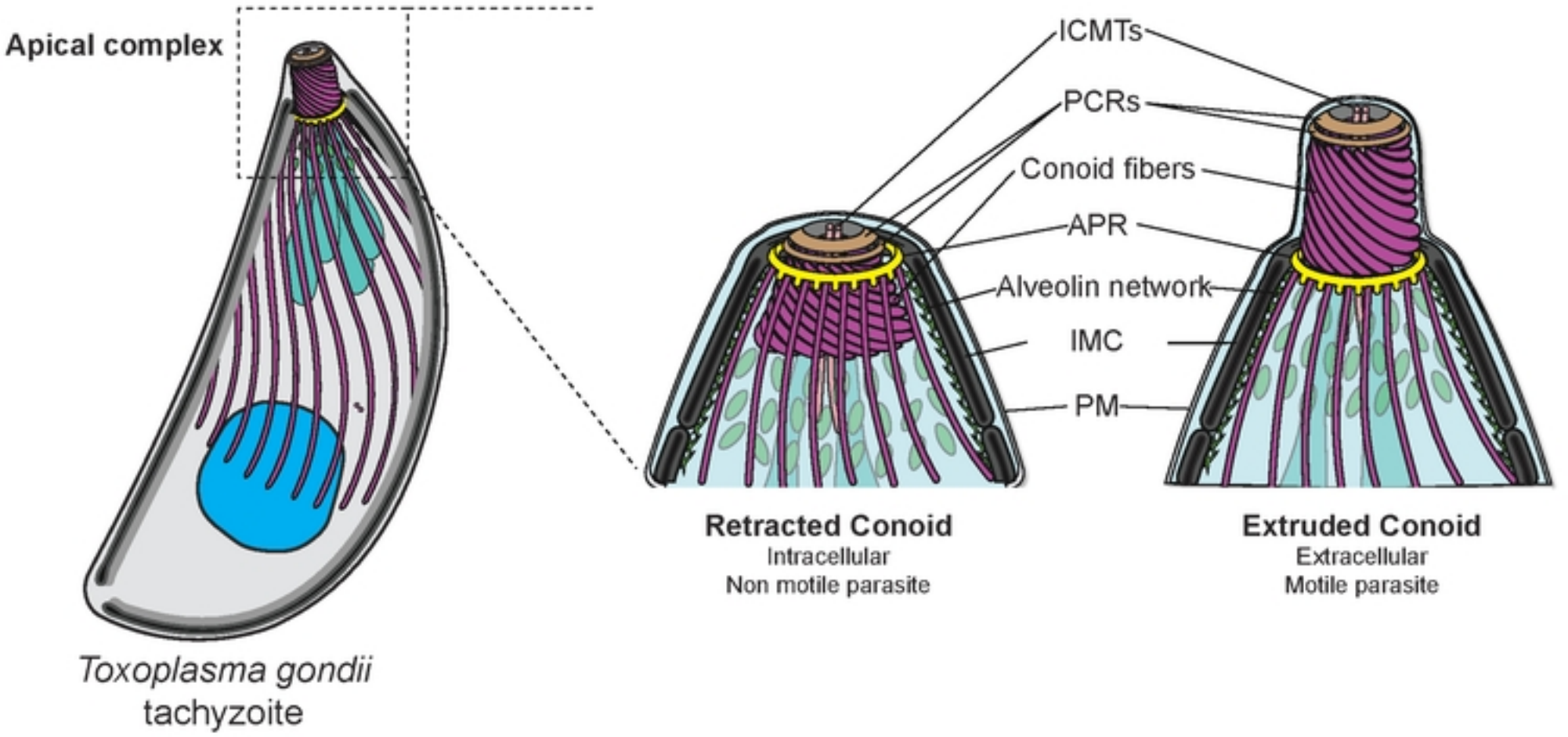
Apical complex
ICMTs
PCRs
Conoid fibers
APR
Alveolin network
IMC
PM
Retracted Conoid
Intracellular
Non motile parasite
Extruded Conoid
Extracellular
Motile parasite
Toxoplasma gondii
tachyzoite

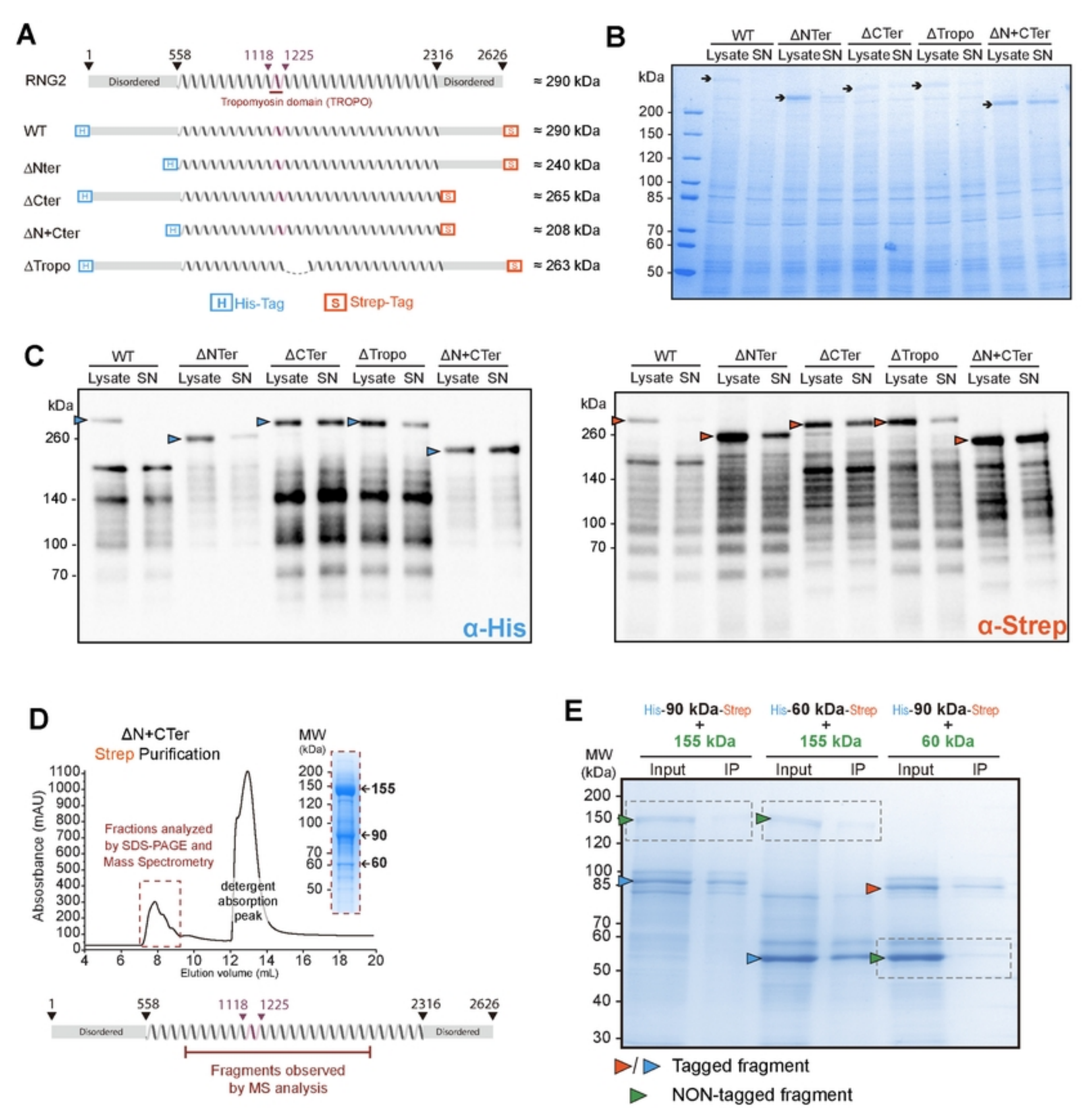
A
1
558
1118
1225
2316
2626
RNG2
Disordered
Disordered
≈ 290 kDa
Tropomyosin domain (TROPO)
WT
ΔNter
ΔCter
ΔN+Cter
ΔTropo
≈ 290 kDa
≈ 240 kDa
≈ 265 kDa
≈ 208 kDa
≈ 263 kDa
His-Tag
Strep-Tag
B
WT
ΔNTer
ΔCTer
ΔTropo
ΔN+CTer
Lysate SN
kDa
200
150
120
100
85
70
60
50
C
α-His
α-Strep
D
ΔN+CTer
Strep Purification
MW (kDa)
155
90
60
Absorbance (mAU)
Fractions analyzed by SDS-PAGE and Mass Spectrometry
detergent absorption peak
Elution volume (mL)
Fragments observed by MS analysis
E
His-90 kDa-Strep + 155 kDa
His-60 kDa-Strep + 155 kDa
His-90 kDa-Strep + 60 kDa
Input
IP
Tagged fragment
NON-tagged fragment

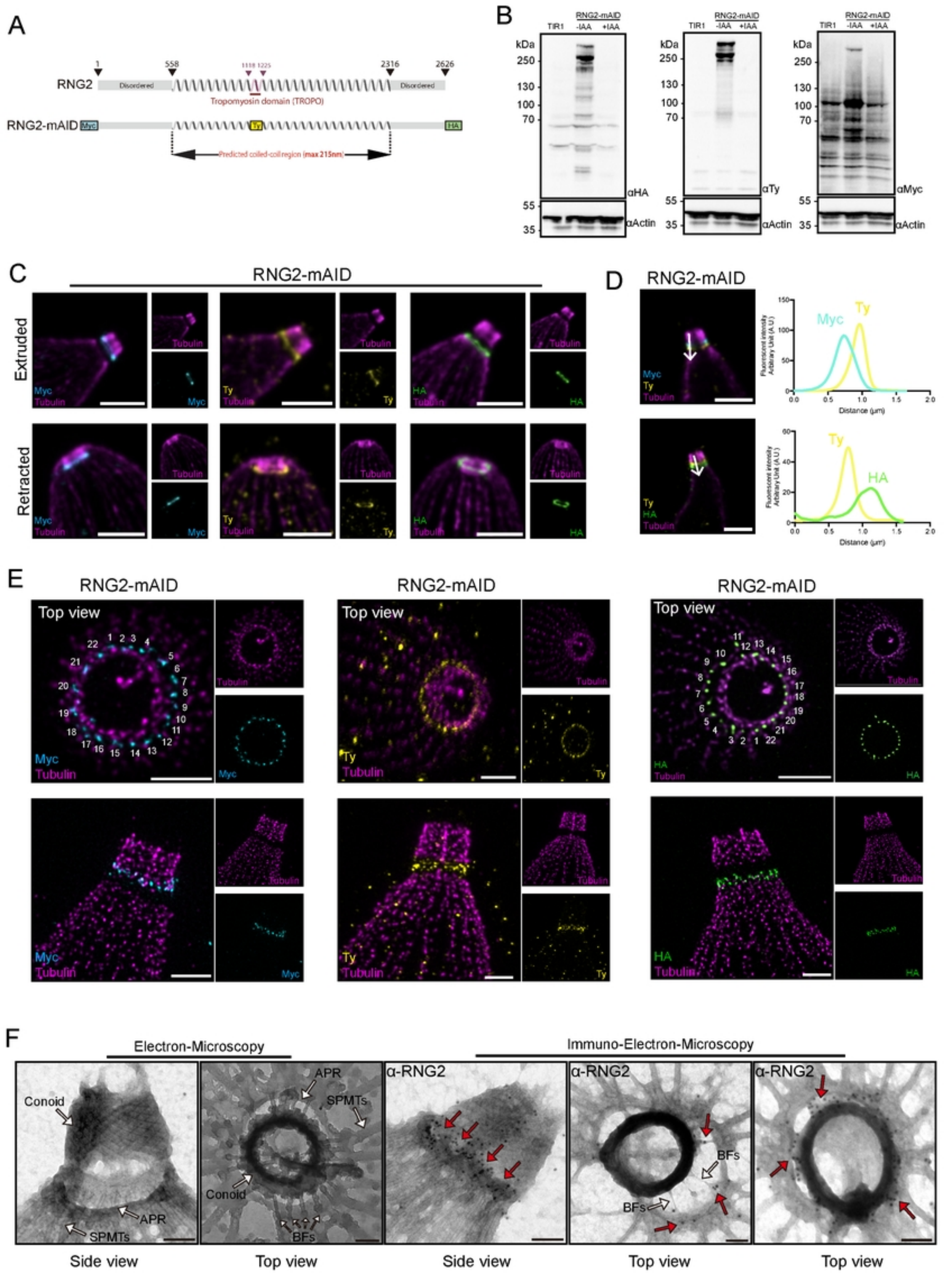
A
RNG2
Disordered
Tropomyosin domain (TROPO)
RNG2-mAID
Myc
Ty
HA
Predicted coiled-coil region (max 215nm)
B
TIR1
RNG2-mAID
-IAA
+IAA
kDa
αHA
αTy
αMyc
αActin
C
RNG2-mAID
Extruded
Retracted
Tubulin
Myc
Ty
HA
D
RNG2-mAID
Fluorescent intensity Arbitrary Unit (A.U.)
Distance (µm)
E
RNG2-mAID
Top view
F
Electron-Microscopy
Immuno-Electron-Microscopy
Conoid
APR
SPMTs
BFs
α-RNG2
Side view
Top view

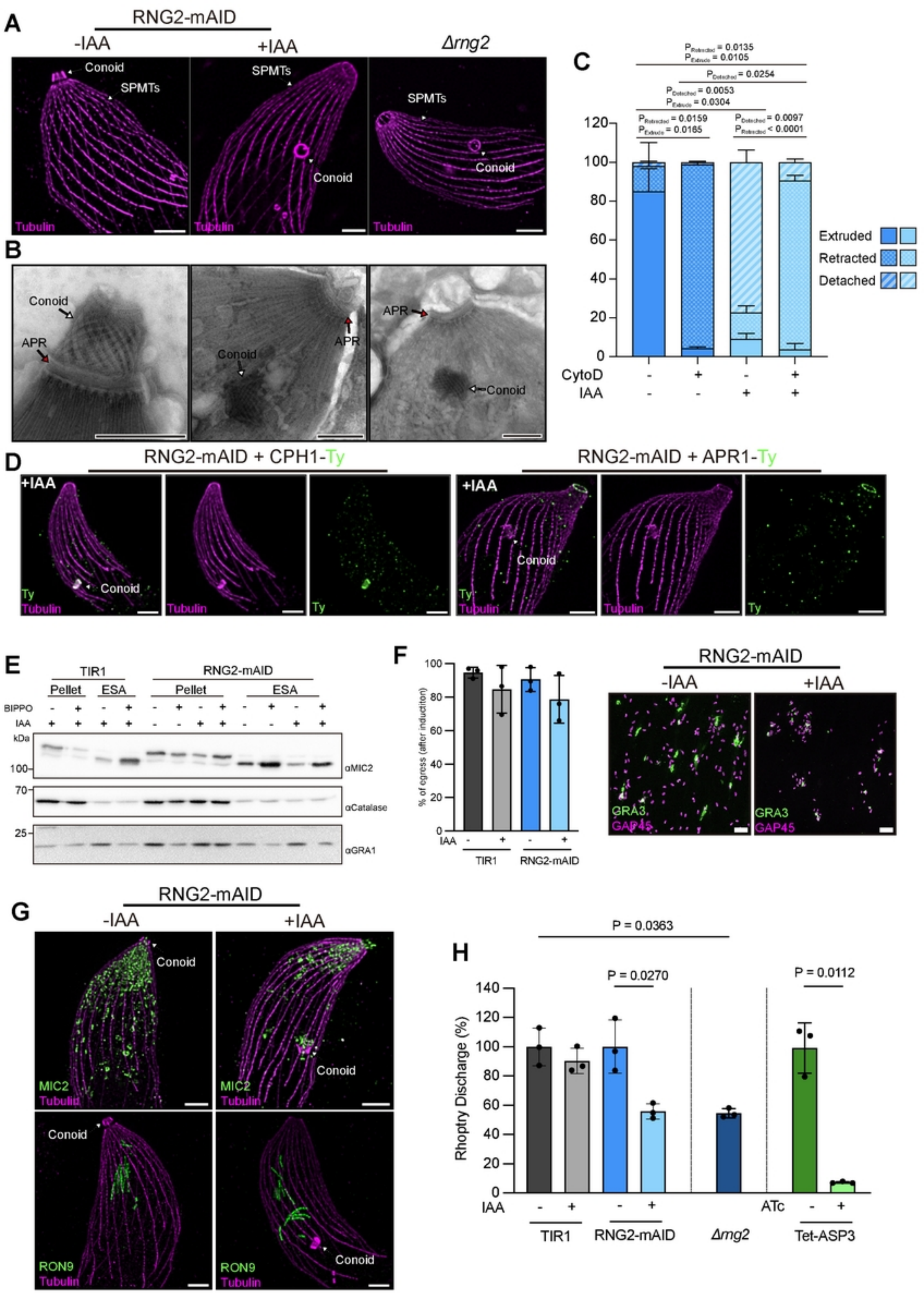
A
RNG2-mAID
-IAA
+IAA
Δrng2
Conoid
SPMTs
Tubulin
B
Conoid
APR
C
P = 0.0135
P = 0.0105
P = 0.0254
P = 0.0053
P = 0.0304
P = 0.0159
P = 0.0165
P = 0.0097
P < 0.0001
Extruded
Retracted
Detached
CytoD
IAA
D
RNG2-mAID + CPH1-Ty
RNG2-mAID + APR1-Ty
+IAA
Ty
Tubulin
E
TIR1
RNG2-mAID
Pellet
ESA
BIPPO
IAA
kDa
αMIC2
αCatalase
αGRA1
F
% of egress (after induction)
TIR1
RNG2-mAID
GRA3
GAP45
G
MIC2
RON9
H
P = 0.0363
P = 0.0270
P = 0.0112
Rhoptry Discharge (%)
ATc
Δmg2
Tet-ASP3

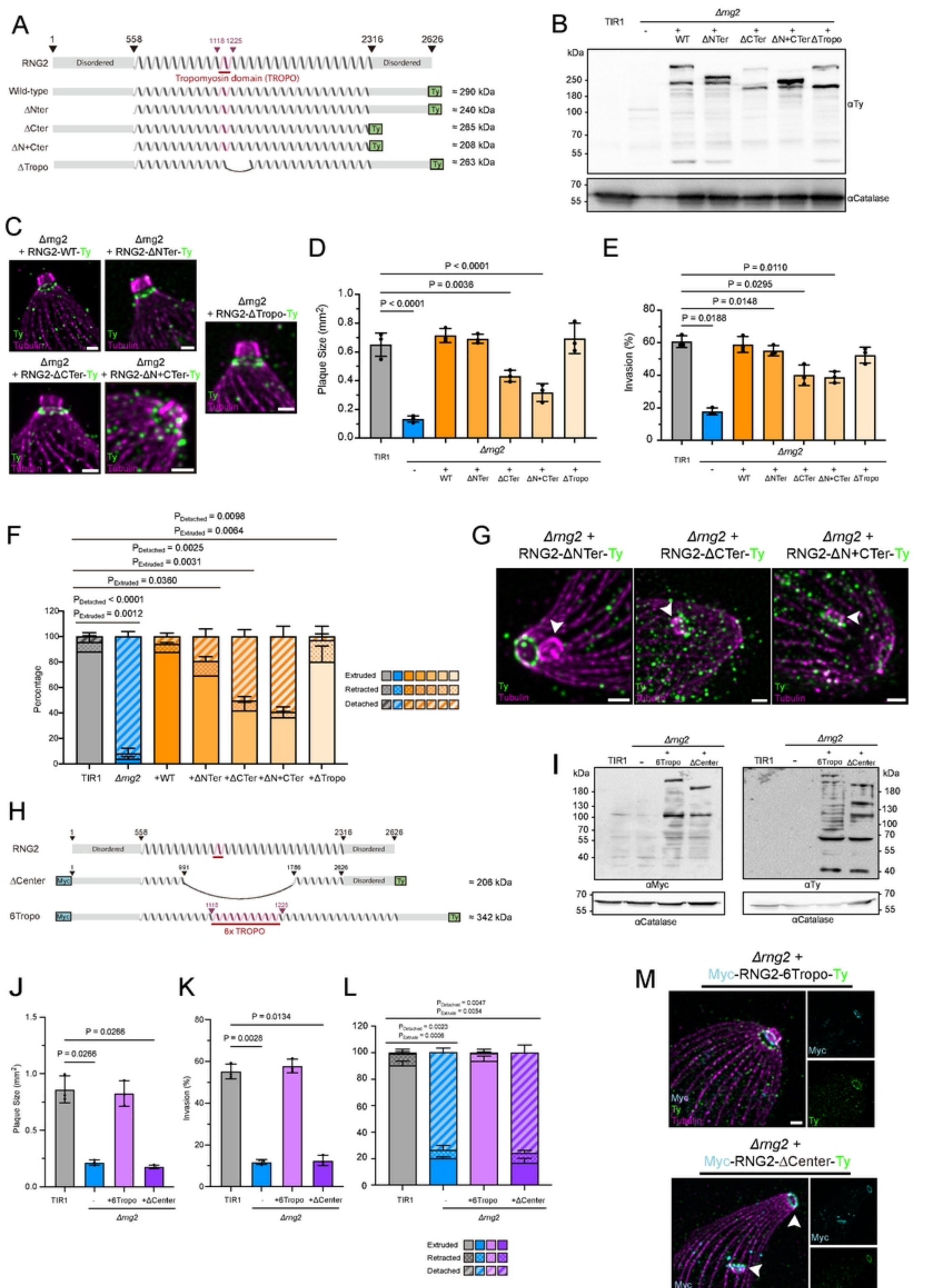
A
RNG2
Disordered
Tropomyosin domain (TROPO)
Wild-type
ΔNter
ΔCter
ΔN+Cter
ΔTropo
= 290 kDa
≈ 240 kDa
≈ 265 kDa
≈ 208 kDa
≈ 263 kDa
B
TIR1
Δmg2
WT
ΔNTer
ΔCTer
ΔN+CTer
ΔTropo
kDa
αTy
αCatalase
C
Δmg2 + RNG2-WT-Ty
Δmg2 + RNG2-ΔNTer-Ty
Δmg2 + RNG2-ΔTropo-Ty
Δmg2 + RNG2-ΔCTer-Ty
Δmg2 + RNG2-ΔN+CTer-Ty
Ty
Tubulin
D
Plaque Size (mm²)
P < 0.0001
P = 0.0036
P < 0.0001
E
Invasion (%)
P = 0.0110
P = 0.0295
P = 0.0148
P = 0.0188
F
Percentage
Extruded
Retracted
Detached
TIR1
Δmg2
+WT
+ΔNTer
+ΔCTer
+ΔN+CTer
+ΔTropo
G
Δmg2 + RNG2-ΔNTer-Ty
Δmg2 + RNG2-ΔCTer-Ty
Δmg2 + RNG2-ΔN+CTer-Ty
H
RNG2
ΔCenter
6Tropo
Myc
Ty
= 206 kDa
≈ 342 kDa
6x TROPO
I
6Tropo
ΔCenter
αMyc
αTy
αCatalase
J
Plaque Size (mm²)
P = 0.0266
P = 0.0266
K
Invasion (%)
P = 0.0134
P = 0.0028
L
+6Tropo
+ΔCenter
M
Δmg2 + Myc-RNG2-6Tropo-Ty
Δmg2 + Myc-RNG2-ΔCenter-Ty

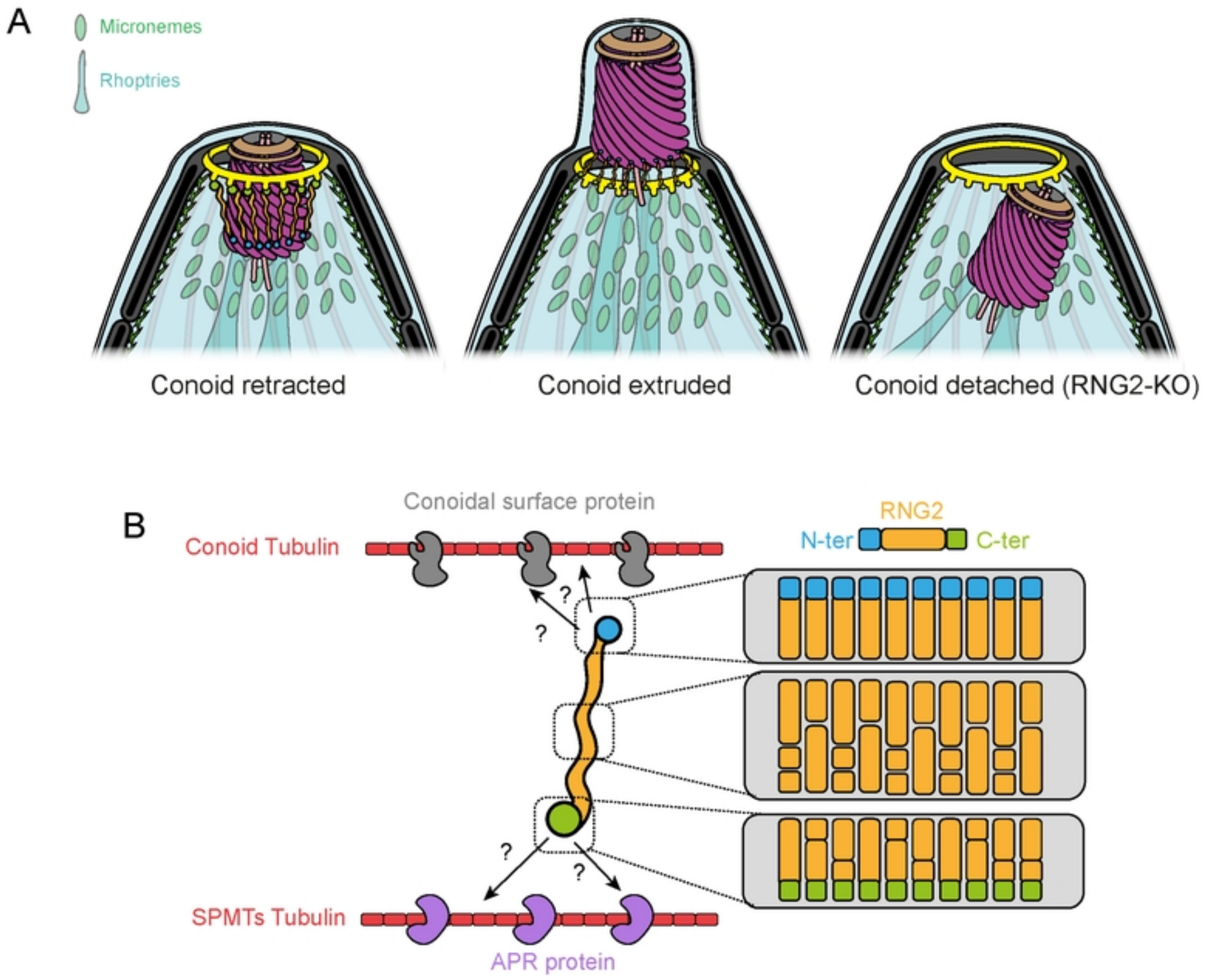
A
Micronemes
Rhoptries
Conoid retracted
Conoid extruded
Conoid detached (RNG2-KO)
B
Conoidal surface protein
Conoid Tubulin
RNG2
N-ter
C-ter
?
?
?
?
SPMTs Tubulin
APR protein